Taylor & Francis
Taylor & Francis Group

Vehicle System Dynamics
International Journal of Vehicle Mechanics and Mobility

ISSN: 0042-3114 (Print) 1744-5159 (Online) Journal homepage: http://www.tandfonline.com/loi/nvsd20

Optimal tyre usage for a Formula One car

A. J. Tremlett & D. J. N. Limebeer

To cite this article: A. J. Tremlett & D. J. N. Limebeer (2016) Optimal tyre usage for a Formula One car, Vehicle System Dynamics, 54:10, 1448-1473, DOI: 10.1080/00423114.2016.1213861

To link to this article: http://dx.doi.org/10.1080/00423114.2016.1213861

VEHICLE SYSTEM DYNAMICS, 2016
VOL. 54, NO. 10, 1448–1473
http://dx.doi.org/10.1080/00423114.2016.1213861

IAVSD
Taylor & Francis
Taylor & Francis Group

Optimal tyre usage for a Formula One car

A. J. Tremlett and D. J. N. Limebeer

Department of Engineering Science, University of Oxford, Oxford, UK

ABSTRACT

Variations in track temperature, surface conditions and layout have led tyre manufacturers to produce a range of rubber compounds for race events. Each compound has unique friction and durability characteristics. Efficient tyre management over a full race distance is a crucial component of a competitive race strategy. A minimum lap time optimal control calculation and a thermodynamic tyre wear model are used to establish optimal tyre warming and tyre usage strategies. Lap time sensitivities demonstrate that relatively small changes in control strategy can lead to significant reductions in the associated wear metrics. The illustrated methodology shows how vehicle setup parameters can be optimised for minimum tyre usage.

ARTICLE HISTORY
Received 25 August 2015
Revised 23 April 2016
Accepted 31 May 2016

KEYWORDS
Thermal tyre model; tyre wear; numerical optimal control; pseudospectral methods; laptime simulation; Formula One car modelling

1. Introduction

Modern racing tyres have evolved to produce tyre forces that are significantly larger than their passenger vehicle counterparts. This has been achieved through stiffer carcass constructions and the use of softer elastomeric rubber compounds.[1,2] These compounds operate at elevated temperatures and offer superior levels of friction, but at the cost of reduced durability. Variations in track surface roughness and ambient temperature, which is encountered at various race venues, have led tyre manufacturers to develop a range of compounds, each with their own friction–durability characteristics. These are commonly referred to as *low* or *high working range* tyres, and reflects the difference in operating temperature required to use them most effectively. Racing regulations [3] dictate that a number of compounds must be used at each race, requiring careful tyre management between pit stops. An area which has come to the fore in recent years is the requirement to 'tyre save' during some race stints. This is done to maintain the frictional properties of the tyres, and to gain a strategic advantage in terms of potential overtaking opportunities. Tyre saving whilst optimising lap times has therefore become a crucial element of a competitive race strategy.

The reliance of friction generation on the compound's viscoelastic properties has been examined by several authors [4–6] in the context of tyre modelling. These studies are based on the seminal work of Grosch,[7] who demonstrated that the adhesive and hysteretic components of friction can be characterised by a single, frequency-dependant master curve. The time–temperature equivalence described in [8] uses a scaling factor to correct these

CONTACT A. J. Tremlett anthony.tremlett@eng.ox.ac.uk

master curves for temperature variations. This method has been widely adopted as a means of representing the temperature–friction relationship of slick racing tyres. These elements are combined in [4] with a lumped parameter thermodynamic model to predict the evolution of tread, carcass and inflation gas temperatures for multiple laps of the Silverstone National Circuit. A finite horizon, nonlinear program is used to find the static optimal track and tyre temperatures for a minimum lap time.

Moore [9] examines fatigue, abrasion and roll formation wear mechanisms for road car rubber compounds. In the case of slick racing tyres in combination with rough track surfaces, abrasion is dominant, and under extreme operating conditions *graining* can occur.[1] A qualitative assessment of this process is presented in [10], which highlights the importance of the frequency of road asperity inputs on the resulting rubber stiffness and wear resistance. The large body of experimental work that is summarised in [11–13] illustrates that rubber temperature, relative slip velocity, normal load and the topology of abrasive surfaces are all key features. These experiments have traditionally been conducted on laboratory rubber block test specimens. The extrapolation of wear metrics to vehicular tyre wear tests [14,15] has proved more challenging however, due to variations in driving style and road surface conditions. As a result, wear models used in vehicle handling simulations must be derived from an extensive series of tyre wear tests.

In this paper, the thermal characteristics of racing compounds and their durability are brought together in a minimum lap time, optimal control setting. The focus of this work is to investigate how the vehicle control history and car setup can be tailored to improve the temperature distribution between tyres, and provide greater insight into efficient tyre saving strategies. In Sections 2 and 2.1 a parameterised, thermodynamic tyre model is presented and validated against on-track surface tyre temperature measurements. This is used in combination with a magic formula tyre model [16] (see Appendix 2) to give a realistic temperature–friction dependence in Section 2.2. Surface tyre temperature and frictional power generated at the contact patch form the inputs to a wear model which is presented in Section 3. These tyre-specific elements are incorporated into a car and track model of the type described in [17,18]. Consequently, only a brief summary of these are given in Section 4 and Appendix 1. Section 5 summarises the mathematical background behind the optimal control methodology employed. The optimisation results are divided into three sections: Section 6.1 deals with a tyre warming strategy to keep each tyre in its optimum temperature range for maximum grip. Section 6.2 includes results on tyre saving strategies by constraining the permissible wear of each tyre over a lap distance. Finally, Section 6.3 demonstrates how temperature and wear models can be used to determine optimal vehicle setup parameters. In this case, differential setup is chosen as this is known to influence tyre wear significantly. Conclusions are presented in Section 7.

2. Thermodynamic tyre model

The thermal behaviour of the tyre surface temperature is modelled using a lumped parameter model that describes the heat flux through the isotropic thermal tyre mass. The dominant heat flows considered in the analysis are shown schematically in Figure 1 and consist of the following:

(i) Q_1 – heat generation in the sliding region of the contact patch
(ii) Q_2 – heat generation due to tyre carcass deflection

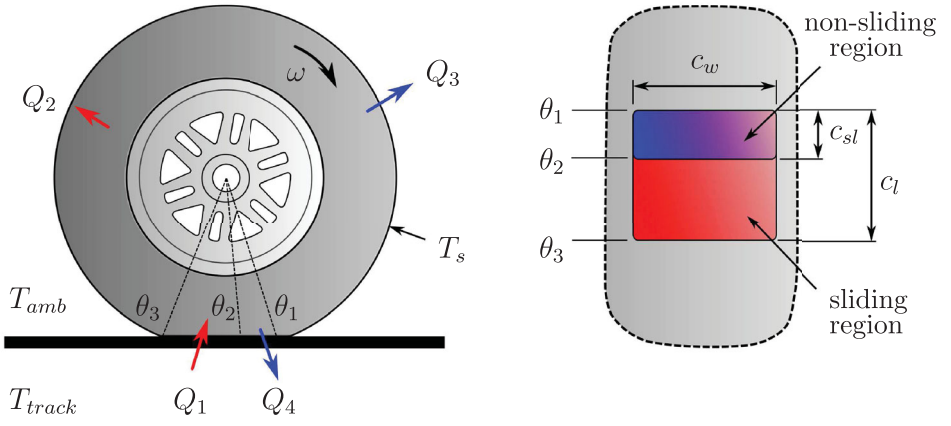

Figure 1. (Left) Dominant heat flows that determine the tyre tread surface temperature T_s. The angle θ_1 defines the angle at which ground contact is first made with the non-sliding region of the contact patch. The angle θ_2 defines the start of the sliding region, whilst θ_3 marks the end of ground contact. (Right) View from the bottom of the tyre detailing the contact patch geometry.

(iii) Q_3 – convective cooling through ambient air surrounding tyre
(iv) Q_4 – conductive cooling in the non-sliding region of the contact patch

The tyre tread surface temperature, T_s, is described by

$$m_t c_t \frac{d}{dt} T_s(t) = Q_1 + Q_2 - Q_3 - Q_4, \tag{1}$$

where c_t is the specific heat capacity of the tyre tread and m_t its mass. The heat generated from the sliding region of the contact patch is calculated through summation of longitudinal and lateral slip powers

$$Q_1 = p_1 u_n (|F_x \kappa| + |F_y \tan \alpha|), \tag{2}$$

where the slip quantities α, κ, and the tyre forces F_x, F_y, are derived from the magic formula model detailed in Appendix 2. The longitudinal velocities, u_n, at each wheel corner are defined by

$$u_{n,rr} = u - \dot{\psi} w_r, \tag{3}$$
$$u_{n,rl} = u + \dot{\psi} w_r, \tag{4}$$
$$u_{n,fr} = \cos\delta(u - \dot{\psi} w_f) + \sin\delta(\dot{\psi} a + v), \tag{5}$$
$$u_{n,fl} = \cos\delta(\dot{\psi} w_f + u) + \sin\delta(\dot{\psi} a + v). \tag{6}$$

The reader is referred to Appendix 1 for definitions of the variables u, v, ψ, w_f, w_r, a and δ. The parameter p_1 accounts for the proportion of frictional power lost to the track in the sliding region of the contact patch. Heat generation due to bulk tyre deflection is treated in a manner similar to that described in [4], with the parameters $p_2 - p_4$ describing efficiency

terms. These relate to the magnitude of heat generated as a result of longitudinal, lateral and normal tyre forces

$$Q_2 = u_n(p_2|F_x| + p_3|F_y| + p_4|F_z|). \tag{7}$$

The convective cooling of each tyre through the ambient air temperature, T_{amb}, is dealt with using a Newtonian cooling law

$$Q_3 = p_5 u^{p_6}(T_{\text{s}} - T_{\text{amb}}), \tag{8}$$

where the heat transfer coefficient term $p_5 u^{p_6}$ is a nonlinear function of the vehicle speed [19] and parameters p_5 and p_6 are used to control the variation in air flow seen between each corner of the vehicle. The conductive cooling through the non-sliding region of the contact patch is determined by

$$Q_4 = h_{\text{t}} A_{\text{cp}}(T_{\text{s}} - T_{\text{track}}), \tag{9}$$

where h_{t} is the heat transfer coefficient between the track and tyre, A_{cp} the non-sliding area of the contact patch and T_{track} the track temperature. The width of the front and rear contact patches assumes constant values c_{wf}, c_{wr}, with the length c_{l} defined by a power function of the normal load

$$c_{\text{l}} = a_{\text{cp}} {F_z}^{0.7}. \tag{10}$$

The empirical constant a_{cp} can be altered to reflect differences between front and rear contact patch length deformation. The non-sliding region length c_{sl}, is related to the total contact patch length c_{l}, by the factor c_{s} where $c_{\text{sl}} = c_{\text{s}}(\alpha)c_{\text{l}}$. The function $c_{\text{s}}(\alpha)$ controls the relative proportion of sliding and non-sliding regions as the vehicle approaches its cornering limit. It is calculated through linear interpolation between the reference values c_{s1} and c_{s2} and the reference slip angle α_c

$$c_{\text{s}}(\alpha) = \frac{\alpha}{\alpha_c}(c_{\text{s2}} - c_{\text{s1}}) + c_{\text{s1}}. \tag{11}$$

The resulting non-sliding front and rear contact patch areas are then calculated using

$$A_{\text{cpf}} = c_{\text{wf}} c_{\text{s}} c_{\text{l}}, \tag{12}$$

$$A_{\text{cpr}} = c_{\text{wr}} c_{\text{s}} c_{\text{l}}. \tag{13}$$

Finally, the independent time variable t, in Equation (1) can be changed to the elapsed track distance s, using

$$\frac{\mathrm{d}T_{\text{s}}}{\mathrm{d}s} = S_f(s)\dot{T}_{\text{s}}, \tag{14}$$

where $S_f(s)$ is the inverse of the car's velocity component along the track spine.[18] The tyre parameters used in this paper are summarised in Table 1.

Table 1. Thermal tyre model input parameters.

Symbol	Description	Units	Value
T_{amb}	Track air temperature	°C	25
T_{track}	Track surface temperature	°C	35
m_t	Tyre tread mass	kg	0.5
c_t	Specific heat capacity of tread	kJ/kg K	1.8
h_t	Heat transfer coefficient (tyre–track contact)	kW/m^2 K	12
c_{wf}	Contact patch width (front)	m	0.20
c_{wr}	Contact patch width (rear)	m	0.22
a_{cp}	Contact patch length constant	m/kN	0.056
α_c	Reference sliding/non-sliding slip angle	°	8
c_{s1}	Sliding/non-sliding reference 1	–	0.3
c_{s2}	Sliding/non-sliding reference 2	–	0.8

2.1. Parameter fitting

The six parameters p_1 through p_6 are determined using a least-squares optimal control calculation in which the following performance index is minimised

$$J = \int_{s_0}^{s_f} (T_s - T_m)^2 \, ds. \tag{15}$$

The variable T_m represents a set of averaged tyre surface temperature measurements taken around a lap of the 'Circuit de Cataluya' in Barcelona. The resulting parameter values for each tyre are detailed in Table 2. In Figure 2, a comparison of the measured and fitted temperature histories is shown. The root mean square (RMS) error of each data set is shown above and in general, an acceptable level of correlation is seen for all tyres, with a maximum RMS error of 6.5°C. It should be noted that whilst differences between front and rear tyre parameters are to be expected due to different tyre sizes, variations between left and right tyre parameters are also seen. This is influenced by a number of factors including tyre wear, heat cycle history and airflow differences between tyre positions. These are factors which can vary during the lap distance and should be borne in mind when applying this parameter fitting approach.

2.2. Temperature–friction sensitivity

The sensitivity of the tyre friction to tread temperature is represented by the scaling factor λ_g, which is a function of the tyre temperature and is given by

$$\begin{aligned}\lambda_g(T_s) = {} & (g_1 T_s + g_2) + (0.5 + 0.5 \sin(\arctan(g_s(T_s - t_{p1}))))(1 - (g_1 T_s + g_2)) \\ & + (0.5 + 0.5 \sin(\arctan(g_s(T_s - t_{p2}))))((g_3 T_s + g_4) - 1).\end{aligned} \tag{16}$$

Table 2. Thermal tyre model parameter optimisation summary.

Tyre	p_1	p_2	p_3	p_4	p_5	p_6
Front left	0.455	0.001	0.011	0.022	0.011	2.170
Front right	0.321	0.001	0.026	0.020	0.605	1.256
Rear left	0.404	0.017	0.001	0.008	0.058	1.603
Rear right	0.382	0.019	0.001	0.010	0.040	1.816

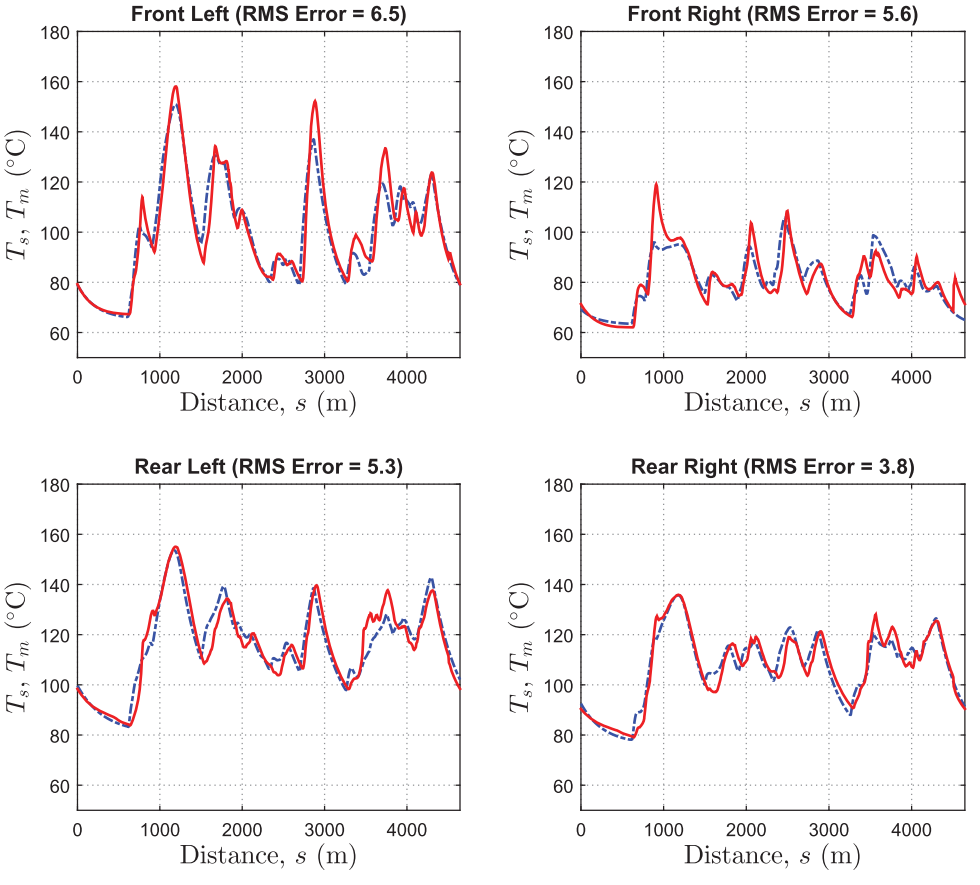

Figure 2. Overlay of average tyre surface temperature measurement T_m (shown in red), against fitted model values T_s (shown in dotted blue). RMS error values shown in °C.

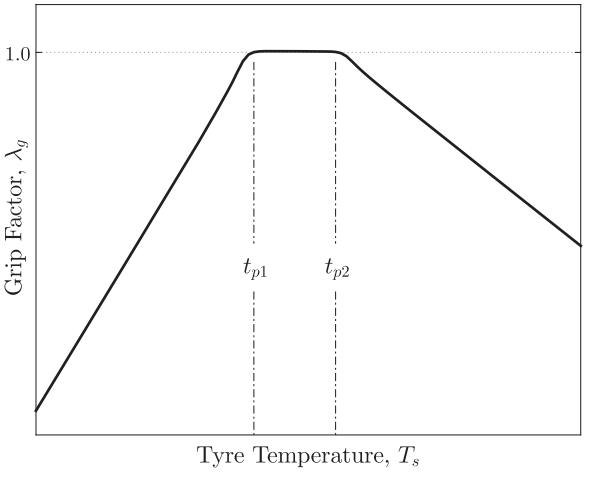

Figure 3. Example of friction factor (λ_g) against tyre temperature (T_s).

Peak friction is achieved between the temperatures t_{p1} and t_{p2}, with the 'fall off' determined by the slope constants g_1 to g_4. The variable g_s controls the sharpness of transition between each of these regions. The resultant longitudinal and lateral tyre forces are scaled by λ_g in Equations (A15) and (A16) detailed in Appendix 2. An example of the temperature–friction function is shown in Figure 3.

3. Wear model

In describing a suitable wear model (for a slick racing tyre), a distinction must first be made between various wear mechanisms. The first is the mechanical abrasion of the compound due to interaction with the track asperities. Chemical degradation of the rubber is another type of degradation mechanism that occurs over multiple racing laps. This is due to the continuation of the vulcanisation process [1] from sustained thermal and stress cycling, which leads to a gradual hardening of the compound, and a reduction in peak friction capability. The results presented in this work focus on the influence of abrasive wear over a single lap, with chemical degradation assumed negligible.

The dependence of abrasion on the frictional energy developed at the contact patch has been documented in several places.[11,14,20] A power law relationship has been successfully used to fit experimental results for synthetic styrene-butadiene (SBR) co-polymers commonly used to manufacture racing compounds. The wear rate $\dot{w}_p$ (expressed in mm/s) as a result of the frictional power, Q_1, can be expressed as

$$\dot{w}_p(Q_1) = w_{p1}\left(\frac{Q_1}{Q_{ref}}\right)^{w_{p2}}, \tag{17}$$

where w_{p1} and w_{p2} represent empirical constants derived from the work detailed in [14] for an SBR compound. The constant Q_{ref} is the reference frictional power at which wear measurements were taken. Tread temperature also plays a significant role in abrasion resistance and previous works have established the existence of an optimum temperature at which minimum wear occurs.[10,12] In the racing context, temperature also determines the likelihood of the compound suffering from the phenomena of *graining* and *blistering*. If a tyre is overworked by the driver when still cold, particles of rubber can break away from the tread surface, increasing wear rates and reducing friction capability (the interested reader is referred to the qualitative analysis of graining presented in [10]). Conversely, if the tyre overheats, blisters can form in localised hot spots over the tread surface, leading to a more extreme increase in wear. To reflect these wear mechanisms, the temperature influence has been split into two regions either side of an optimum temperature t_{tp}, at which minimum wear occurs. A working surface temperature range of 60–160°C is considered. The propensity of the rubber to graining in the range $60^\circ\text{C} < T_s < t_{tp}$ can be described by

$$\dot{w}_g(T_s) = w_{g1}(T_s - t_{tp})^{w_{g2}}. \tag{18}$$

Similarly, the propensity of the compound to blister in the region $t_{tp} < T_s < 160^\circ\text{C}$

$$\dot{w}_b(T_s) = w_{b1}(T_s - t_{tp})^{w_{b2}}. \tag{19}$$

The parameters $w_{g1}, w_{g2}, w_{b1}, w_{b2}$ are designed to allow the relative severity of graining and blistering wear mechanisms to be tailored to the specific compound chemistry. This process

is well understood by tyre manufacturers who can effect substantial changes in these wear mechanisms through the proportion and composition of carbon black rubber fillers and vulcanising agents.[1] A final expression describing the total wear rate $\dot{w}_a$ is formed as a continuous function of $\dot{w}_p$, $\dot{w}_g$ and $\dot{w}_b$. Linear superposition of each wear mechanism is assumed to describe the total wear rate as

$$\dot{w}_a(T_s, Q_1) = (\dot{w}_g + \dot{w}_p) + (0.5 + 0.5\sin(\arctan(g_s(T_s - t_{tp}))))((\dot{w}_b + \dot{w}_p) - (\dot{w}_g + \dot{w}_p)). \tag{20}$$

Example wear rate characteristics are shown in Figure 4 for the model parameters summarised in Table 3. Equation (20) can be expressed in terms of the elapsed distance as

$$\frac{dw_a}{ds} = S_f(s)\dot{w}_a. \tag{21}$$

The total wear, w_t, at the end of a lap for a single tyre can then be found by evaluating the integrand

$$w_t = \int_{s_0}^{s_f} S_f(s)\dot{w}_a \, ds, \tag{22}$$

where s_0 and s_f define the start and end elapsed distances of the lap.

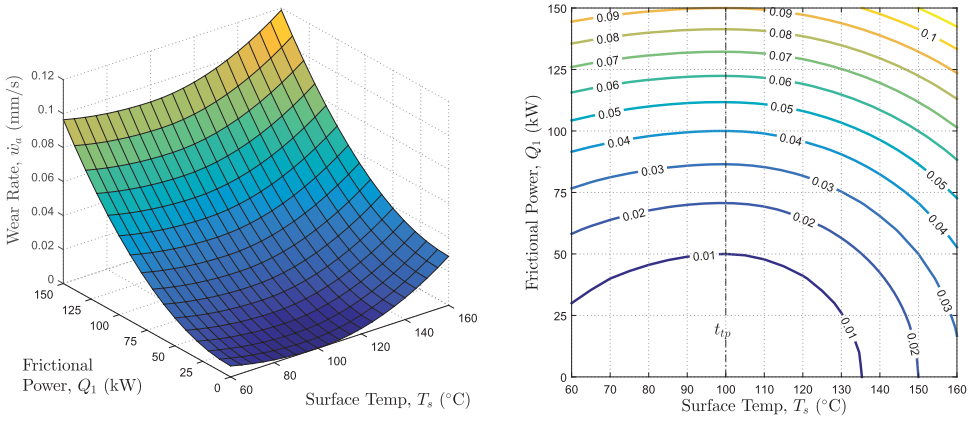

Figure 4. Wear rate $\dot{w}_a$ (in mm/s) shown as a function of the frictional power Q_1 and surface temperature T_s. Wear rate contours are shown in right-hand figure, with the dotted black trace delineating the graining–blistering transition temperature t_{tp}.

Table 3. Tyre wear model parameters.

Symbol	Description	Units	Value
w_{g1}	Graining gain factor	mm/°C s	0.4×10^{-5}
w_{g2}	Graining exponent	–	2
w_{b1}	Blistering gain factor	mm/°C s	0.8×10^{-5}
w_{b2}	Blistering exponent	–	2
w_{p1}	Frictional power gain factor	mm/s	0.09
w_{p2}	Frictional power exponent	–	1.6
Q_{ref}	Reference frictional power	kW	150
t_{tp}	Minimum wear temperature transition	°C	100

4. Vehicle and track model

The vehicle and track model used in this paper is an extension of one described elsewhere [17,18,21] and is consequently only included in Appendix 1 for the reader's reference. The track and car kinematics are modelled using ideas from classical differential geometry. The car model is standard and is based on a rigid-body representation of a chassis with longitudinal, lateral and yaw freedoms. The tyre description given in [18] is used in combination with upgraded wear and thermal models. Tyre and vehicle parameters are given in Appendices 2 and 3.

5. Optimal control

The general-purpose optimal control problem solver (GPOPS)-II [22] is used to perform the calculations presented. In broad terms, the problem, along with its associated boundary, input and state constraints is converted into a large, sparse, nonlinear programming problem.[23] GPOPS-II is based on direct pseudospectral discretisation, which uses Legendre–Gauss–Radau collocation and Radau's integration formula.[24] In this framework, the state and controls are treated as decision variables on a finite implicit integration mesh. A solution of minimum lap time optimal control problems using trapezoidal integration can be found in [18]. The solution of similar problems, using GPOPS-II, is described in [17], where the background control theory and some of the solution practicalities are also discussed. The practicalities associated with solving minimum lap time optimal control problems are also discussed in [21].

6. Results

The study presented in this paper is based on minimum-time optimal laps of the 'Circuit de Cataluya' in Barcelona, shown in Figure 5. The track has 16 corners with their approximate distances from the start–finish (SF) detailed in Table 4. The vehicle, tyre and aerodynamic parameters used in the analysis are given in Appendix 1 and 3. In the sections that follow, the influence of the thermodynamic tyre model is first examined by considering optimal tyre warming effects. Tyre saving control strategies, now commonplace in Formula 1, are then investigated through the introduction of appropriate wear constraints. Finally, an example of how wear metrics can be used to determine optimal vehicle setup parameters is presented. The particular case of the differential viscosity is chosen, since this has a significant influence on tyre wear.

6.1. Tyre warming strategy

To demonstrate the influence of temperature on tyre friction, a preliminary investigation into an optimal tyre warming strategy is conducted. A high working range tyre is chosen in which peak friction is developed between $t_{p1} = 110^{\circ}$C and $t_{p2} = 130^{\circ}$ C. The tyre temperatures are set arbitrarily to 20°C at the start of the lap. A baseline case is considered with temperature sensitivity effectively disabled by setting $\lambda_g = 1$ for the entirety of the lap. A secondary case allows temperature sensitivity to influence tyre force generation as described in Section 2.2.

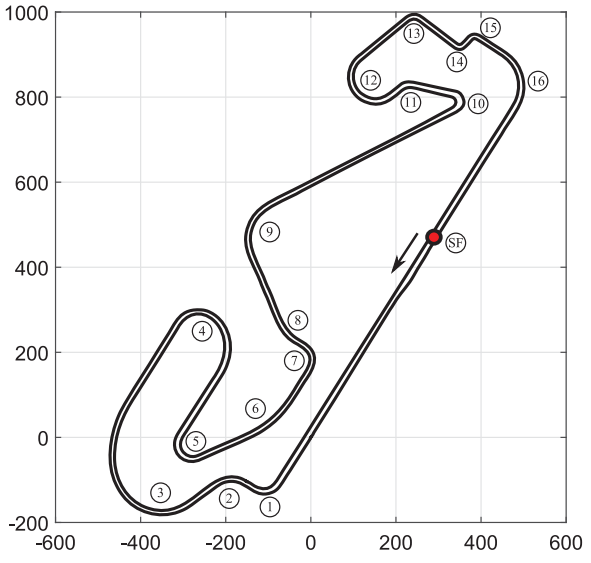

Figure 5. Plan view of the 'Circuit de Cataluya' (Barcelona) with corner numbers and the start–finish line (SF). The axis distances are in metres.

Table 4. Approximate distances to mid corner on the 'Circuit de Catalunya' track (in metres from the start–finish line).

Corner	Distance (m)	Corner	Distance (m)
1	725	9	2750
2	800	10	3350
3	1050	11	3500
4	1650	12	3650
5	2000	13	3900
6	2250	14	4000
7	2420	15	4050
8	2500	16	4200

Figure 6 illustrates the tyre temperature history for both cases. The highest tyre surface temperatures are seen on the left-hand tyres, which are subject to the highest normal loads due to the lateral load transfer from a predominance of right-hand corners. The most noticeable differences can be seen on the front tyre temperatures, during the entrance to turn (1) at 500–800 m and again at the entrance to turn (10) at 3200–3500 m.

Inspection of the racing line at both of these points in Figures 7 and 8 reveals that the temperature sensitive case has induced higher surface temperatures through the common practice of 'weaving'. This is shown to be most effective at the end of long straights where the front tyres have cooled sufficiently to fall outside their optimum temperature range.

6.2. Tyre saving strategy

To investigate optimal control strategies that generate acceptable levels of tyre wear over a racing lap, the maximum wear on each tyre is limited by a wear ceiling $w_{t,max}$, which is

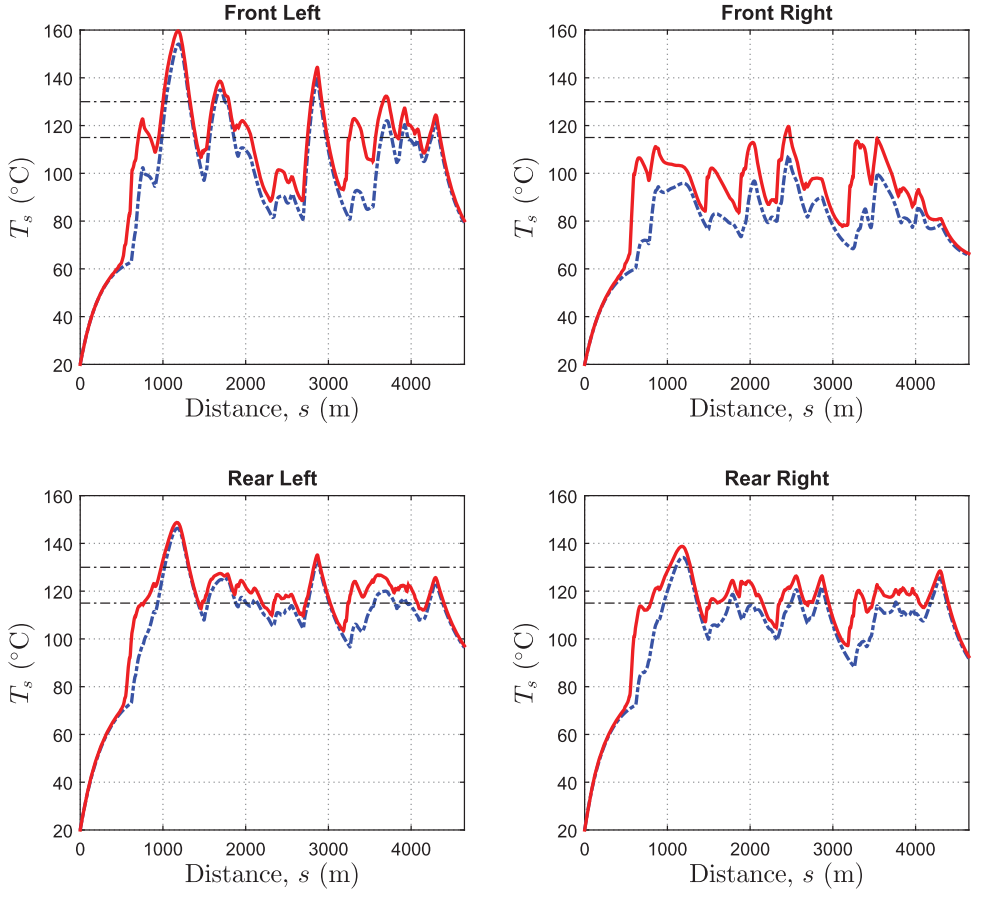

Figure 6. Tyre temperatures with temperature-grip sensitivity disabled ($\lambda_g = 1$) shown in dotted blue trace. The solid red trace shows tyre temperatures with temperature-grip sensitivity enabled (see Equation (16)). The dotted black trace indicates the optimum temperature range for maximum friction.

imposed by the following inequality constraints

$$w_{\mathrm{t,max}} - w_{\mathrm{t,fl}} \geq 0, \tag{23}$$

$$w_{\mathrm{t,max}} - w_{\mathrm{t,fr}} \geq 0, \tag{24}$$

$$w_{\mathrm{t,max}} - w_{\mathrm{t,rl}} \geq 0, \tag{25}$$

$$w_{\mathrm{t,max}} - w_{\mathrm{t,rr}} \geq 0. \tag{26}$$

A baseline case is considered for a low working range tyre, where $t_{\mathrm{p1}} = 90^{\circ}\mathrm{C}$ and $t_{\mathrm{p2}} = 105^{\circ}$ C, with the associated wear model parameters summarised in Table 3. The wear constraint is effectively free in the baseline case by setting $w_{\mathrm{t,max}}$ to an arbitrarily high value (5 mm in this instance). The resulting velocity profile for this configuration is shown in Figure 9 and generates a lap time of 81.245 s. The total wear on each of the tyres at the end of the lap is detailed in Table 5 and confirms that the left-hand tyres are under the greatest burden. These have worn by approximately 0.3 mm when compared to the 0.18 mm associated with the right-hand tyres.

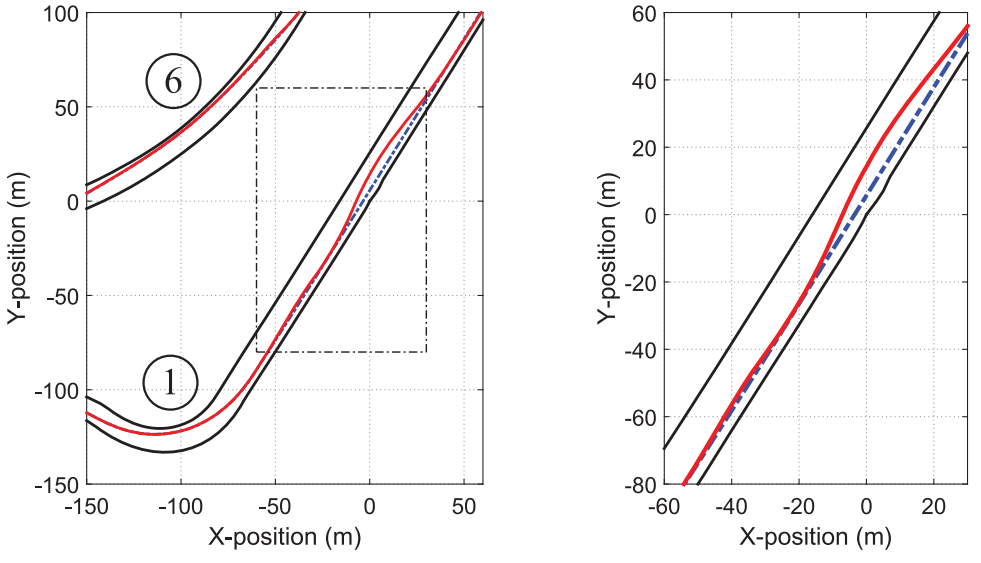

Figure 7. Racing line shown for track section from start–finish straight into turn ①. The dotted blue trace shows the racing line with temperature-grip sensitivity disabled ($\lambda_g = 1$). The solid red trace illustrates the racing line with temperature-grip sensitivity enabled (see Equation (16)).

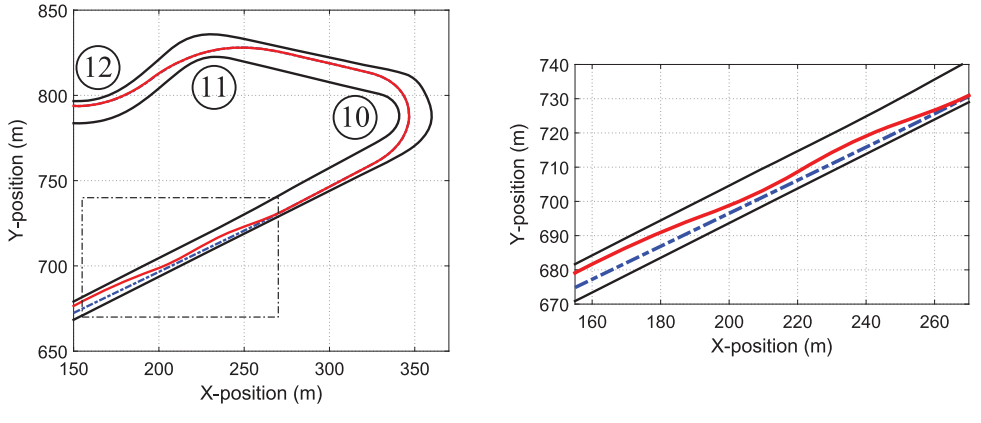

Figure 8. Racing line shown for track section into turns ⑩– ⑫. The dotted blue trace shows the racing line with temperature-grip sensitivity disabled ($\lambda_g = 1$). The solid red trace illustrates the racing line with temperature-grip sensitivity enabled (see Equation (16)).

A key part of any competitive race strategy is the ability to manage multiple race stints on tyres with significantly different friction-wear characteristics. An area which has come to the fore over recent years is the requirement to 'tyre save' during some race stints. This is done not only to maintain the frictional properties of the tyres, but also to gain a strategic advantage in the form of potential overtaking opportunities between pit stops. Tyre saving whilst minimising the lap time is an important consideration. In this work, efficient tyre saving is investigated by constraining the maximum wear (w_t) generated by each of the tyres during a single lap. The results for a second case where $w_{t,max} = 0.23$ mm are shown

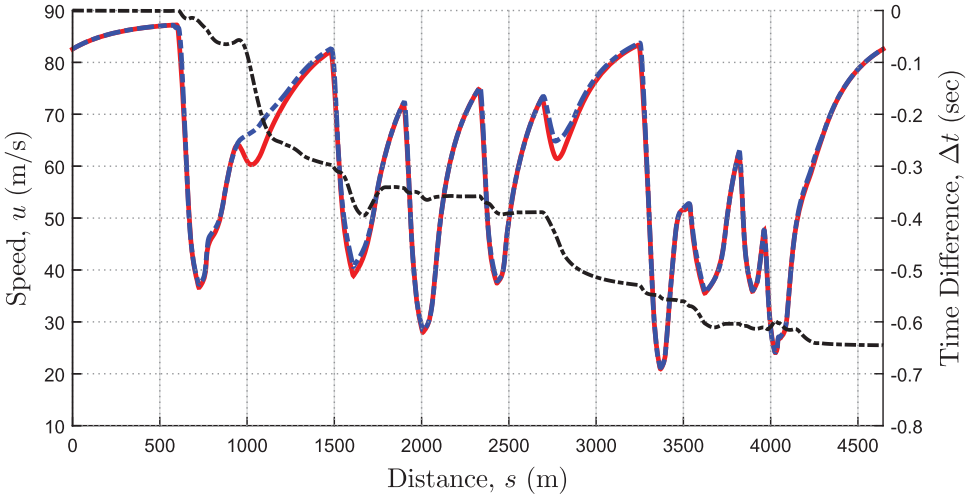

Figure 9. Speed traces over lap distance, illustrating the case with wear constraint $w_{t,max} = 5$ mm in dotted blue, resulting in a lap time of 81.245 s. The solid red trace shows the case when the $w_{t,max} = 0.23$ mm, resulting in a lap time of 81.891 s. The time difference between configurations is shown in dotted black.

Table 5. Resulting tyre wear (in mm) per lap for an unrestricted wear constraint ($w_{t,max} = 5$ mm) and the case where $w_{t,max} = 0.23$ mm.

Tyre position	w_t (mm) $w_{t,max} = 5$	w_t (mm) $w_{t,max} = 0.23$
Front left	0.348	0.188
Front right	0.183	0.229
Rear left	0.300	0.138
Rear right	0.177	0.099
Total	1.008	0.654

in Figure 9, with the resulting tyre wear given in Table 5. What is immediately apparent is that there are two high speed corners on the circuit where the car slows, in turn ③ at 950–1250 m and again at turn ⑨ at 2700–3000 m. The resulting total tyre wear has reduced by 35%, with significant reductions in the more heavily loaded outside tyres. As one might expect, the lap time has increased to 81.891 s.

Inspection of the tyre wear rates over the lap distance in Figure 10 confirms that turns ③ and ⑨ are also the locations for the biggest peaks in wear rate for the two outside tyres. Although the most significant wear reductions can be seen at these points, both rear tyres show smaller reductions at all corners. To help explain how these changes have been brought about, the torque delivery to the rear axle (see Figure 12) is analysed with respect to the first three corners of the circuit, shown in Figure 11. In the first instance, the braking point of the unconstrained case denoted by ● at $s = 609$ m, is approximately 12 m ahead of the constrained configuration braking point at ●. The nature of the torque application is also much smoother as the car transitions from the braking phase into the apex of turn ① at ▽. The torque delivery at the apex of the slower speed turn ② at □ is identical in both cases, but a much larger reduction in applied torque is seen at the apex of turn ③ at △. Similar behaviour is seen at turn ⑨. The general practice of earlier, smoother braking and

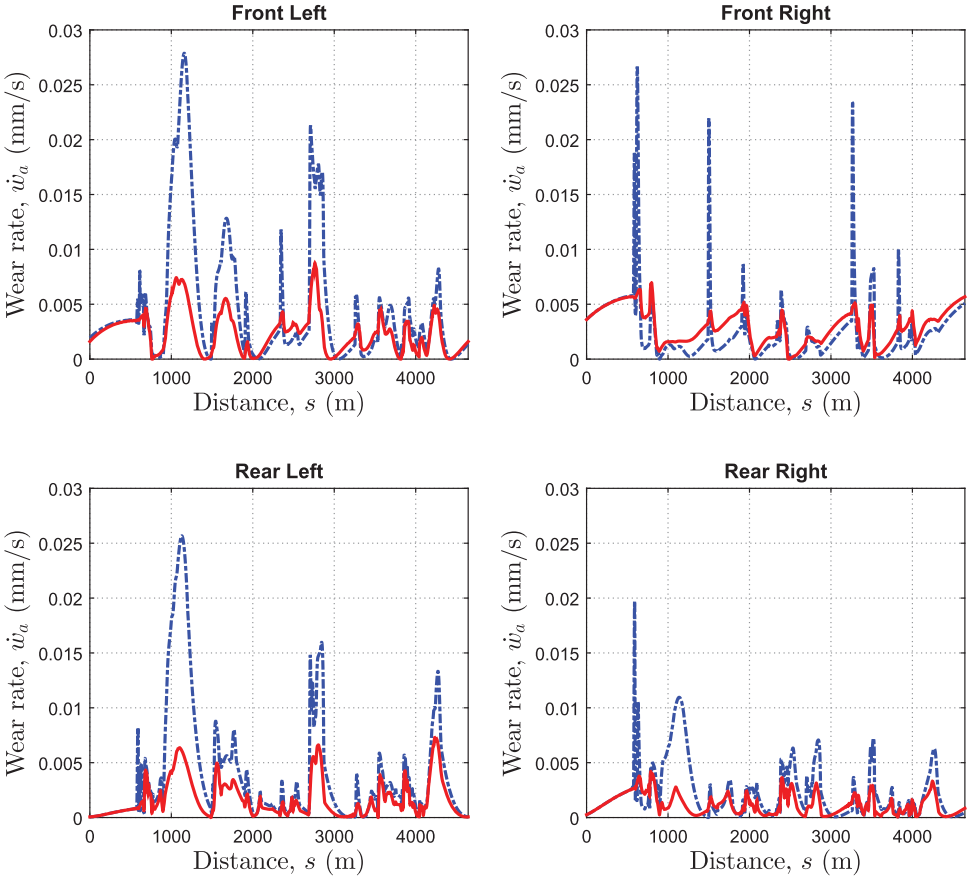

Figure 10. Tyre wear rate $\dot{w}_a$ with wear constraint $w_{t,max} = 5$ mm, shown for each tyre in dotted blue traces. Wear rates in the constrained configuration, where $w_{t,max} = 0.23$ mm are shown in solid red.

reduced throttle inputs during high speed corners is reinforced by the strategies currently used in Formula 1.

The total wear on each tyre by the end of the lap was almost universally reduced in the constrained case (see Table 5). However, a small increase in the front right wear was seen, from 0.18 to 0.23 mm. In the unconstrained configuration, large peaks in wear rate were generated as the tyre approached lock-up under severe braking (see Figure 10). The smoother braking profile of the tyre saving strategy has significantly reduced these peaks, but this is countered by the tyre starting to fall below its optimum temperature for minimum wear ($t_{tp} = 100^\circ$ C). This can be witnessed in its temperature profile in Figure 13, and gives some insight into the challenges of bringing all four tyres into their optimum operating window at the same time. Although this will potentially make the tyre more susceptible to graining, the wear of all four tyres is more evenly balanced, with the total wear reduced by 35%.

The resulting minimum lap time for a number of constraint cases are detailed in Figure 14, where $w_{t,max}$ ranges from 0.23 to 0.33 mm in steps of 0.005 mm. The percentage total tyre saving (i.e. reduction seen in the total wear of all four tyres) when compared to

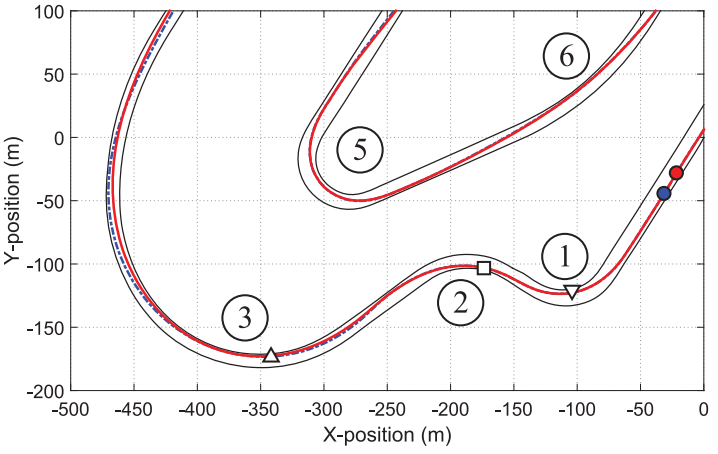

Figure 11. Racing line shown for track section between turns ① and ③. Unconstrained configuration shown in dotted blue, with solid red trace illustrating the constrained case. Braking points into turn ① denoted by 🔴, 🔵, with apexes of turns ①– ③ denoted by ▽, □ and △.

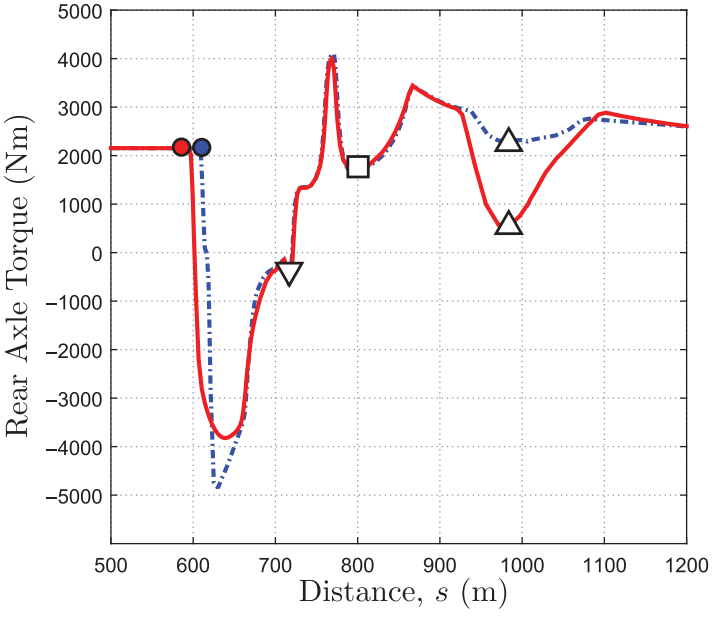

Figure 12. Total torque delivered to rear tyres between turns ① and ③. Unconstrained configuration shown in dotted blue, with solid red trace illustrating the constrained case. Braking points into turn ① denoted by 🔴, 🔵, with apexes of turns ①– ③ denoted by ▽, □ and △.

the unconstrained baseline case is also shown. It is interesting to note that whilst tyre saving displays an approximately linear relationship with $w_{\mathrm{t,max}}$, the resulting minimum lap time shows a diminished return in terms of 'buying' lap time reductions with tyre wear. For the case of $w_{\mathrm{t,max}} = 0.29$ mm, the total tyre wear saving is 13%, which is accompanied by only a 0.05 s increase in lap time. This suggests that relatively small changes in driving strategy can impact tyre saving considerably, without significant increases to lap time. This

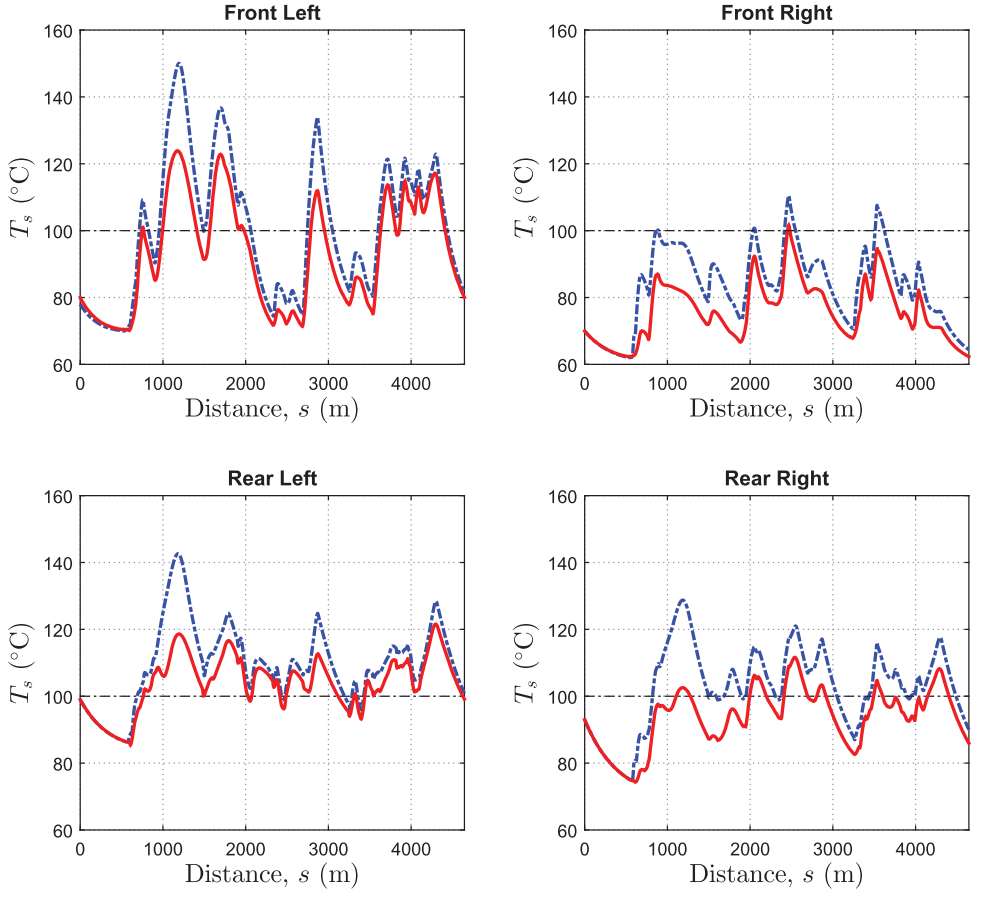

Figure 13. Tyre surface temperature T_s with wear constraint $w_{t,max} = 5$ mm shown in dotted blue traces. Tyre temperatures in the constrained configuration ($w_{t,max} = 0.23$ mm) are shown in solid red. The optimum tyre temperature for minimum wear t_{tp} is shown in dotted black.

is borne out through experience, where it is known that some drivers are much easier on their tyres than others, whilst ultimately no slower in raw lap time terms.

6.3. Differential configuration example

In Sections 6.1 and 6.2 driving strategies that help to warm tyres and minimise associated wear were presented. In the following section, the potential to tailor the car's setup to minimise tyre wear is also investigated. To illustrate this process the differential setup is chosen, as it is known to influence tyre wear significantly.[25,26]

Three configurations are considered, the first being an 'open' setup that delivers equal torque to each of the driven wheels that are free to rotate independently. This is achieved by setting $k_d = 0$ N/rpm (see Equation (A12) in Appendix 1). Similarly, a 'locked' configuration is achieved by setting $k_d = 5000$ N/rpm in Equation (A12), which forces the rear wheels to rotate at equal speed. Experience has shown that locked differentials allow the vehicle to accelerate more aggressively out of corners, but can also produce excessive tyre

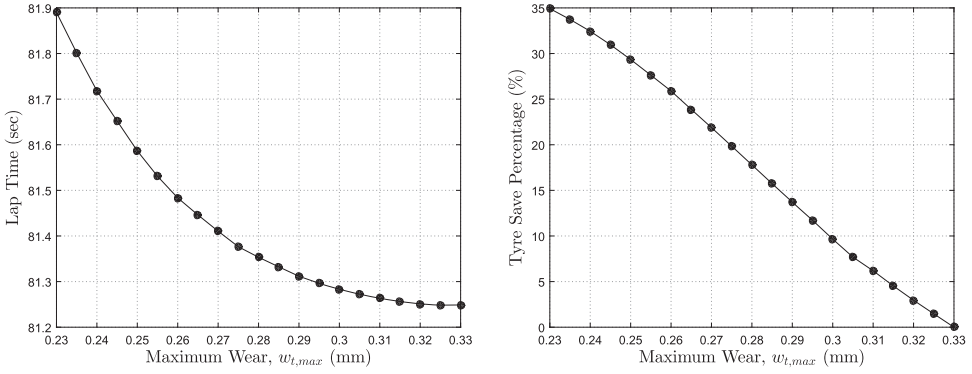

Figure 14. Variation in minimum lap time with wear constraint $w_{t,max}$ shown in left-hand plot. The right-hand plot shows the percentage total tyre saving (of all four tyres) when compared to the baseline case when $w_{t,max} = 5$ mm (total tyre wear of baseline is equal to 1.008 mm – see Table 5).

wear.[25] This relates to the lack of driven wheel speed independence, as the inner and outer wheels attempt to track different path radii in corners. Conversely, the open differential allows the driven wheels to track at different speeds with no additional tyre scrub. The downside of the open differential is the limited traction achievable on corner exits, due to lateral load transfer (away from the inside wheels).[25,26]

The solution to this problem has been the development of semi-active differentials, which can transition between open and locked states almost instantaneously [2] (termed 'limited slip differentials' or simply LSD). Regulations require that these must be controlled by a limited set of vehicle parameters, in a predetermined, lookup table style control strategy.[3] A torque bias between driven wheels is typically generated through a hydraulic piston clamping a clutch plate assembly.[2] This LSD configuration can be represented by the introduction of the hydraulic pressure control variable H_p, and a modified version of Equation (A12) in which

$$R(F_{lrx} - F_{rrx}) = -\frac{2}{3}\frac{H_p \hat{\mu}_p z_f}{A_p}\left(\frac{r_o^3 - r_i^3}{r_o^2 - r_i^2}\right), \tag{27}$$

where A_p is the actuator piston area, z_f the number of friction faces, and r_i and r_o are, respectively, the inner and outer radii of the clutch surfaces. The variable $\hat{\mu}_p$ relates to the friction coefficient of the clutch material μ_p, and maintains the correct torque transfer direction for the LSD case

$$\hat{\mu}_p = \mu_p(\sin(\arctan(\omega_{lr} - \omega_{rr}))). \tag{28}$$

The optimal LSD pressure H_p for a lap of the Barcelona circuit is shown in Figure 15. The resulting tyre wear and lap times for open, locked and LSD configurations are also detailed in Table 6. In all cases, tyre temperature and wear models have been enabled, with the wear constraint $w_{t,max} = 5$ mm.

Table 6 illustrates that the biggest difference in the tyre wear occurs between open and locked configurations on the rear tyres. Specifically, the outside rear left wears significantly more with a locked differential (0.44 mm), than with its open differential counterpart

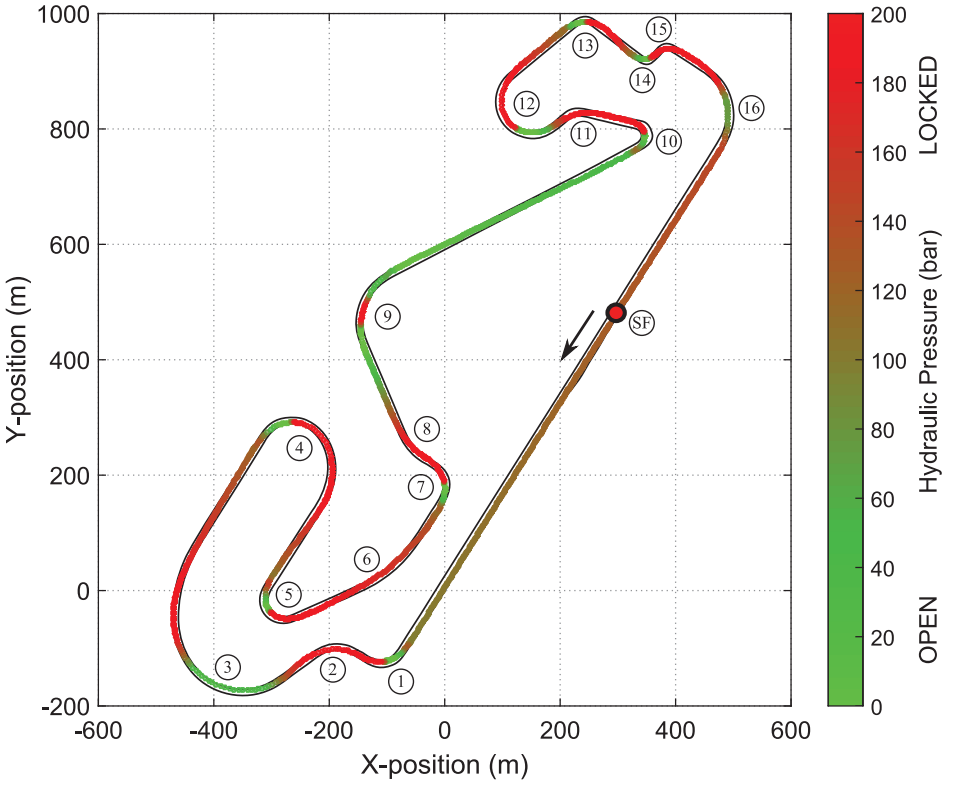

Figure 15. Plan view of the 'Circuit de Cataluya' (Barcelona) illustrating colour contour of optimal LSD hydraulic pressure trace, H_p. Green regions denote areas in which the differential is 'open', with the red areas indicating when the differential is 'locked'.

Table 6. Resulting tyre wear (in mm) per lap for open ($k_d = 0$ N/rpm), locked ($k_d = 5000$ N/rpm) and optimal LSD differential configurations.

Tyreposition	Open	LSD	Locked
Front left wear (mm)	0.353	0.327	0.325
Front right wear (mm)	0.184	0.185	0.185
Rear left wear (mm)	0.277	0.398	0.439
Rear right wear (mm)	0.170	0.185	0.195
Lap time (s)	81.385	80.323	80.504

(0.28 mm). This is attributable to the induced scrub of the rear tyres as the locked axle attempts to negotiate a corner. This is reinforced in Figure 16, which indicates significant differences between turns ④ and ⑤ (1500–2000 m) and during the tight series of corners between turns ⑪ and ⑭ (3500–4000 m).

In raw lap time terms, the locked differential provides greater traction out of corners, and hence a quicker lap time of 80.504 s, when compared to 81.385 s in the open case. The LSD provides a further lap time reduction to 80.323 s. The work presented in [26] demonstrates that this performance gain is due to an increase in the vehicle's lateral acceleration capability at corner apexes. This is confirmed in Figure 15, which establishes the general trend of opening the differential on corner entry, but quickly locking on corner exit, to

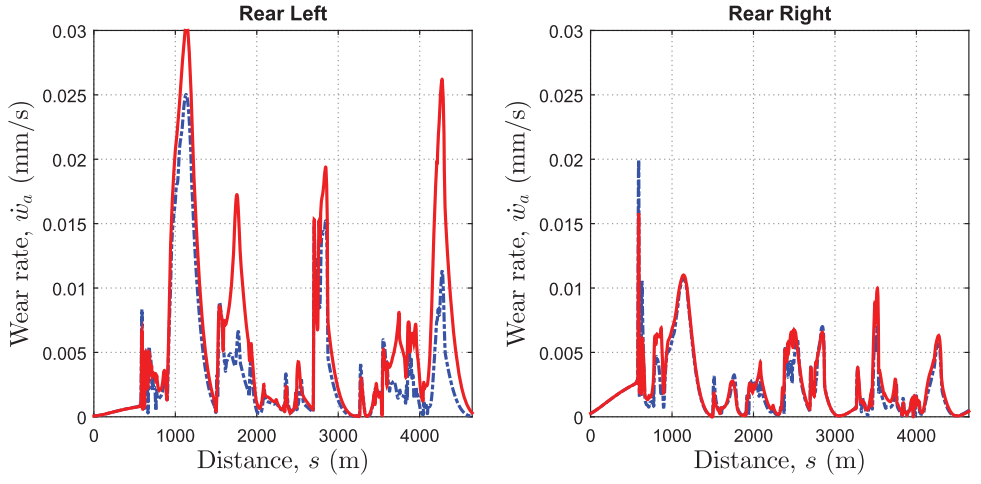

Figure 16. Rear tyre wear rates ($\dot{w}_a$) for the open differential case in dotted blue, and for a locked differential configuration in solid red.

maximise traction and longitudinal acceleration. Importantly, the 'opening up' of the differential on corners has prevented unwanted tyre scrub and brought with it a reduction in associated tyre wear (when compared to the locked case in Table 6).

7. Conclusion

The management of the friction–durability trade off for racing tyres is a crucial part of competitive race strategies. In order to gain insight into the management of this trade off a tyre surface temperature model was developed and validated with experimental measurements. This thermal model was then combined with a wear model, which used both surface temperature and contact patch frictional power to predict tyre wear over a racing lap. Pseudospectral optimal control was used to 'drive the car' so as to optimise the tyre friction and minimise lap times whilst extending the tyres' life. The results suggest that earlier, smoother braking into corners, and lower throttle inputs on high speed corner apexes, gives the most efficient tyre usage. Finally, the method illustrated how tyre wear metrics could also help determine optimal vehicle setup parameters. This is illustrated for the particular case of the differential, but could be applied in much the same way to other vehicle setup parameters.

Disclosure statement

No potential conflict of interest was reported by the authors.

Funding

This work was supported in part by the UK Engineering and Physical Sciences Research Council.

References

[1] Haney P. The racing & high-performance tire. Warrendale (PA): SAE International; 2003.
[2] Wright P. Formula One technology. Warrendale (PA): SAE International; 2001.
[3] Fédération Internationale de l'Automobile. 2015 formula one technical regulations. Tech. Rep.; 2015.
[4] Kelly DP. Lap time simulation with transient vehicle and tyre dynamics [PhD thesis]. Cranfield: Cranfield University School of Engineering; 2008.
[5] Fevrier P, Fandard G. A new thermal and mechanical tyre model for handling simulation. 11th international VDI congress, tyres-chassis-road; Oct 23 and 24; Hanover; 2007.
[6] Lorenz B, Persson B, Fortunato G, Giustiniano M, Baldoni F. Rubber friction for tire tread compound on road surfaces. J Phys Condens Matter. 2013;25(9):095007.
[7] Grosch KA. The relation between the friction and visco-elastic properties of rubber. Proc R Soc Lond A: Math Phys Eng Sci. 1963;274(1356):21–39.
[8] Williams ML, Landel RF, Ferry JD. The temperature dependence of relaxation mechanisms in amorphous polymers and other glass-forming liquids. J Am Chem Soc. 1955;77(14):3701–3707.
[9] Moore DF. Friction and wear in rubbers and tyres. Wear. 1980;61(2):273–282.
[10] Persson BNJ, Tosatti E. Qualitative theory of rubber friction and wear. J Chem Phys. 2000;112(4):2021–2029.
[11] Clark S. The pneumatic tire. Washington (DC): U.S. Department of Transportation, National Highway Traffic Safety Administration; 2006.
[12] Schallamach A. Recent advances in knowledge of rubber friction and tire wear. Rubber Chem Technol. 1968;41(1):209–244.
[13] Moore DF. The friction of pneumatic tyres. Oxford: Elsevier Scientific Pub. Co; 1975.
[14] KA Grosch. Correlation between road wear of tires and computer road wear simulation using laboratory abrasion data. Rubber Chem Technol. 2004;77(5):791–814.
[15] Maitre O, Süssner M, Zarak CEvaluation of tire wear performance. SAE Technical Paper 980256; 1998.
[16] Pacejka HB. Tyre and vehicle dynamics. 2nd ed. Oxford: Butterworth-Heinemann; 2008.
[17] Limebeer DJN, Perantoni G, Rao AV. Optimal control of formula one car energy recovery systems. Int J Control. 2014;87(10):2065–2080.
[18] Perantoni G, Limebeer DJ. Optimal control for a formula one car with variable parameters. Veh Syst Dyn. 2014;52(5):653–678.
[19] Browne AL, Wickliffe LE. Parametric study of convective heat transfer coefficients at the tire surface. Tire Sci Technol. 1980;8(3):37–67.
[20] Grosch KA. Abrasion of rubber and its relation to tire wear. Rubber Chem Technol. 1992;65(1):78–106.
[21] Limebeer DJN, Perantoni G. Optimal control of a formula one car on a three-dimensional track part 2: optimal control. ASME J Dyn Syst Meas Control. 2014;137(5):article number 13 p.
[22] Patterson MA, Rao AV. GPOPS-II version 1.0: a general-purpose MATLAB toolbox for solving optimal control problems using the Radau pseudospectral method. Gainesville (FL): University of Florida; 2013.
[23] Betts JT. Practical methods for optimal control and estimation using nonlinear programming. 2nd ed. Philadelphia (PA): SIAM; 2001.
[24] Davis PJ, Rabinowitz P. Methods of numerical integration. Orlando (FL): Academic Press; 1984.
[25] Milliken WF, Milliken DL. Race car vehicle dynamics. Warrendale (PA): SAE; 1995.
[26] AJ Tremlett, Assadian F, DJ Purdy, Vaughan N, AP Moore, Halley M. Quasi-steady-state linearisation of the racing vehicle acceleration envelope: a limited slip differential example. Veh Syst Dyn. 2014;52(11):1416–1442.

Appendix 1. Vehicle model

The vehicle model used in this paper is an extension of one described in [17,18,21]. It is based on a rigid-body representation of a chassis with longitudinal, lateral and yaw freedoms. Each tyre produces longitudinal and lateral forces that are responsive to the tyres' slip. These forces together with the steer and yaw angle definitions are given in Figure A1. The vehicle parameters are given in Table A1 in Appendix 1.

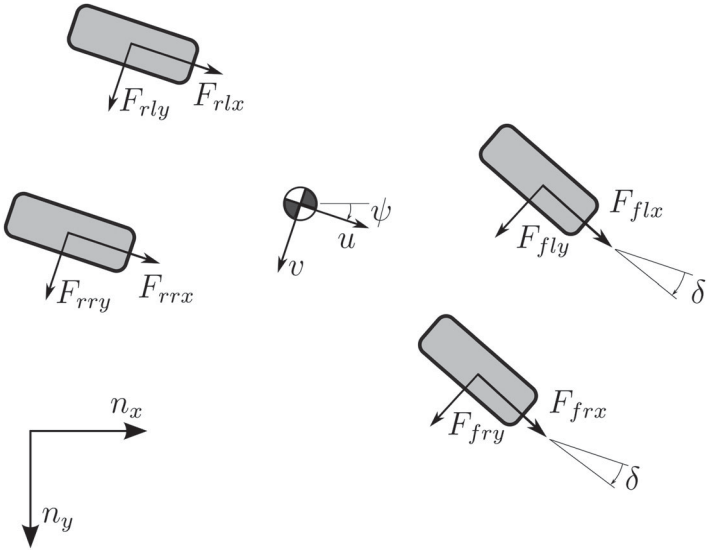

Figure A1. Tyre force system with inertial reference frame, $n_x - n_y$.

Table A1. Vehicle parameters.

Symbol	Description	Value
P_{max}	Peak engine power	560 kW
M	Vehicle mass	660 kg
I_z	Moment of inertia about the z-axis	450 kg m^2
w	Wheelbase	3.4 m
a	Distance of the mass centre from the front axle	1.8 m
b	Distance of the mass centre from the rear axle	$w-a$
h	Centre of mass height	0.3 m
D_{roll}	Roll moment distribution (fraction at the front axle)	0.5
w_f	Front wheel to car centre line distance	0.73 m
w_r	Rear wheel to car centre line distance	0.73 m
R	Wheel radius	0.33 m
k_d	Differential friction coefficient	100 N/rpm

Balancing forces in the longitudinal and lateral directions, whilst also balancing the yaw moments, gives

$$M\frac{\mathrm{d}}{\mathrm{d}t}u(t) = M\omega v + F_x,$$

$$M\frac{\mathrm{d}}{\mathrm{d}t}v(t) = -M\omega u + F_y,$$

$$I_z \frac{\mathrm{d}}{\mathrm{d}t}\omega(t) = a(\cos\delta(F_{\mathrm{fry}} + F_{\mathrm{fly}}) + \sin\delta(F_{\mathrm{frx}} + F_{\mathrm{flx}})) + w_{\mathrm{f}}(\sin\delta F_{\mathrm{fry}} - \cos\delta F_{\mathrm{frx}}) - w_{\mathrm{r}}F_{\mathrm{rrx}} + w_{\mathrm{f}}(\cos\delta F_{\mathrm{flx}} - \sin\delta F_{\mathrm{fly}}) + w_{\mathrm{r}}F_{\mathrm{rlx}} - b(F_{\mathrm{rry}} + F_{\mathrm{rly}}), \tag{A1}$$

where $\omega = \dot{\psi}$, M is the vehicle mass and I_z its moment of inertia in yaw. F_x and F_y are the longitudinal and lateral forces, respectively, acting on the car

$$F_x = \cos\delta(F_{\mathrm{frx}} + F_{\mathrm{flx}}) - \sin\delta(F_{\mathrm{fry}} + F_{\mathrm{fly}}) + (F_{\mathrm{rrx}} + F_{\mathrm{rlx}}) + F_{\mathrm{ax}}, \tag{A2}$$

$$F_y = \cos\delta(F_{\mathrm{fry}} + F_{\mathrm{fly}}) + \sin\delta(F_{\mathrm{frx}} + F_{\mathrm{flx}}) + (F_{\mathrm{rry}} + F_{\mathrm{rly}}), \tag{A3}$$

where F_{ax} is the aerodynamic drag force. These equations can be expressed in terms of the independent variable s as follows:

$$\frac{\mathrm{d}u}{\mathrm{d}s} = S_f(s)\dot{u}, \tag{A4}$$

$$\frac{\mathrm{d}v}{\mathrm{d}s} = S_f(s)\dot{v}, \tag{A5}$$

$$\frac{\mathrm{d}\omega}{\mathrm{d}s} = S_f(s)\dot{\omega}. \tag{A6}$$

A.1 Load transfer

The tyre normal forces are treated as time-varying non-positive inputs normal to the ground plane that must be constrained by the usual laws of mechanics. To this end, forces acting on the car in the n_z direction are balanced, in addition to moments around the lateral and longitudinal body-fixed axes. Balancing the vertical forces gives

$$0 = F_{\mathrm{rrz}} + F_{\mathrm{rlz}} + F_{\mathrm{frz}} + F_{\mathrm{flz}} + Mg + F^{\mathrm{f}}_{\mathrm{az}} + F^{\mathrm{r}}_{\mathrm{az}}, \tag{A7}$$

in which the $F_{..z}$'s are the vertical tyre forces for each of its four wheels, g is the acceleration due to gravity, and $F^{\mathrm{f}}_{\mathrm{az}}$ and $F^{\mathrm{r}}_{\mathrm{az}}$ are the front and rear, respectively, aerodynamic down forces acting on the car. Balancing moments around the car's body-fixed longitudinal axis gives

$$0 = w_{\mathrm{r}}(F_{\mathrm{rlz}} - F_{\mathrm{rrz}}) + w_{\mathrm{f}}(F_{\mathrm{flz}} - F_{\mathrm{frz}}) + hF_y, \tag{A8}$$

in which F_y is the lateral inertial force acting on the car's mass centre (see Equation (A3)). Balancing moments around the car's body-fixed lateral axis gives

$$0 = b(F_{\mathrm{rrz}} + F_{\mathrm{rlz}} + F^{\mathrm{r}}_{\mathrm{az}}) - a(F_{\mathrm{frz}} + F_{\mathrm{flz}} + F^{\mathrm{f}}_{\mathrm{az}}) + hF_x, \tag{A9}$$

where F_x is the longitudinal inertial force acting on the car's mass centre (see Equation (A2)). A unique solution for the tyre loads can be obtained by adding a suspension-related roll balance relationship, in which the lateral load difference across the front axle is some fraction of the whole

$$F_{\mathrm{frz}} - F_{\mathrm{flz}} = D_{\mathrm{roll}}(F_{\mathrm{frz}} + F_{\mathrm{rrz}} - F_{\mathrm{flz}} - F_{\mathrm{rlz}}), \tag{A10}$$

where $D_{\mathrm{roll}} \in [0, 1]$.

A.2 Wheel torque distribution

The braking system applies equal pressure to the brake calipers on each axle, with the braking pressures between the front and rear axles satisfying a static balance ratio. The torque applied to the rear wheels is distributed through a traditional LSD device.

A.2.1 Brakes.

Equal brake caliper pressures are approximated with equal braking torques when neither wheel on a particular axle is locked. If a wheel 'locks up', the braking torque applied to the locked wheel may be lower than that applied to the rolling wheel. For the front wheels this constraint is modelled as follows:

$$0 = \max(\omega_{\mathrm{fr}}, 0)\max(\omega_{\mathrm{fl}}, 0)(F_{\mathrm{fr}x} - F_{\mathrm{fl}x}), \tag{A11}$$

in which ω_{fr} and ω_{fl} are the angular velocities of the front right and front left wheel, respectively. If either road wheel 'locks up', the corresponding angular velocity will be non-positive and the braking torque constraint (A11) will be inactive.

A.2.2 Differential.

The drive torque is delivered to the rear wheels through a LSD, which is modelled by

$$R(F_{\mathrm{lr}x} - F_{\mathrm{rr}x}) = -k_{\mathrm{d}}(\omega_{\mathrm{lr}} - \omega_{\mathrm{rr}}), \tag{A12}$$

in which ω_{lr} and ω_{rr} are the rear wheel angular velocities, R is the wheel radius and k_{d} is a torsional damping coefficient. The special cases of an open and a locked differential correspond to $k_{\mathrm{d}} = 0$ and k_{d} arbitrarily large respectively. Limited slipping occurs between these extremes.

Appendix 2. Tyre friction

The tyre frictional forces are modelled using empirical formulae that are responsive to the tyre normal loads and the combined slip. The tyre's longitudinal slip is described by a longitudinal slip coefficient κ, whilst the lateral slip is described by a slip angle α.[16] Following standard conventions we use

$$\kappa = -\left(1 + \frac{R\omega_n}{u_n}\right), \tag{A13}$$

$$\tan\alpha = -\frac{v_n}{u_n}, \tag{A14}$$

where R is the wheel radius and ω_n the wheel's spin angular velocity. The quantities u_n and v_n are the absolute speed components of the wheel centre in a wheel-fixed coordinate system. The following formulae give the peak values and locations of the lateral and longitudinal friction coefficients using linear interpolation [4]

$$\mu_{x\max} = \lambda_g(F_z - F_{z1})\frac{\mu_{x\max 2} - \mu_{x\max 1}}{F_{z2} - F_{z1}} + \mu_{x\max 1}, \tag{A15}$$

$$\mu_{y\max} = \lambda_g(F_z - F_{z1})\frac{\mu_{y\max 2} - \mu_{y\max 1}}{F_{z2} - F_{z1}} + \mu_{y\max 1}, \tag{A16}$$

$$\kappa_{\max} = (F_z - F_{z1})\frac{\kappa_{\max 2} - \kappa_{\max 1}}{F_{z2} - F_{z1}} + \kappa_{\max 1}, \tag{A17}$$

$$\alpha_{\max} = (F_z - F_{z1})\frac{\alpha_{\max 2} - \alpha_{\max 1}}{F_{z2} - F_{z1}} + \alpha_{\max 1}, \tag{A18}$$

where the quantities containing a '1' or a '2' in the subscript are measured tyre parameters. The tyre slip is normalised with respect to the peak slip

$$\kappa_n = \kappa/\kappa_{\max}, \tag{A19}$$

$$\alpha_n = \alpha/\alpha_{\max}. \tag{A20}$$

Following normalisation, the slip is characterised by a combined-slip coefficient

$$\rho = \sqrt{\alpha_n^2 + \kappa_n^2}. \tag{A21}$$

The friction coefficients in the longitudinal and lateral directions are described by

$$\mu_x = \mu_{x\max} \sin\left(Q_x \arctan(S_x\rho)\right), \tag{A22}$$

$$\mu_y = \mu_{y\max} \sin\left(Q_y \arctan(S_y\rho)\right), \tag{A23}$$

with

$$S_x = \frac{\pi}{2\arctan(Q_x)}, \tag{A24}$$

$$S_y = \frac{\pi}{2\arctan(Q_y)}. \tag{A25}$$

Finally, the longitudinal and lateral components of the tyre forces are given by

$$F_x = \mu_x F_z \frac{\kappa_n}{\rho}, \tag{A26}$$

$$F_y = \mu_y F_z \frac{\alpha_n}{\rho}. \tag{A27}$$

The four wheels slip angles are given by

$$\begin{aligned}
\alpha_{\mathrm{rr}} &= \arctan\left(\frac{v - \dot{\psi} b}{u - \dot{\psi} w_{\mathrm{r}}}\right),\\
\alpha_{\mathrm{rl}} &= \arctan\left(\frac{v - \dot{\psi} b}{u + \dot{\psi} w_{\mathrm{r}}}\right),\\
\alpha_{\mathrm{fr}} &= \arctan\left(\frac{\sin\delta(\dot{\psi} w_{\mathrm{f}} - u) + \cos\delta(\dot{\psi} a + v)}{\cos\delta(u - \dot{\psi} w_{\mathrm{f}}) + \sin\delta(\dot{\psi} a + v)}\right),\\
\alpha_{\mathrm{fl}} &= \arctan\left(\frac{\cos\delta(\dot{\psi} a + v) - \sin\delta(\dot{\psi} w_{\mathrm{f}} + u)}{\cos\delta(\dot{\psi} w_{\mathrm{f}} + u) + \sin\delta(\dot{\psi} a + v)}\right),
\end{aligned} \tag{A28}$$

with the longitudinal slip coefficients given by

$$\begin{aligned}
\kappa_{\mathrm{rr}} &= -\left(1 + \frac{R\omega_{\mathrm{rr}}}{u - \dot{\psi} w_{\mathrm{r}}}\right),\\
\kappa_{\mathrm{rl}} &= -\left(1 + \frac{R\omega_{\mathrm{rl}}}{u + \dot{\psi} w_{\mathrm{r}}}\right),\\
\kappa_{\mathrm{fr}} &= -\left(1 + \frac{R\omega_{\mathrm{fr}}}{\cos\delta(u - \dot{\psi} w_{\mathrm{f}}) + \sin\delta(\dot{\psi} a + v)}\right),\\
\kappa_{\mathrm{fl}} &= -\left(1 + \frac{R\omega_{\mathrm{fl}}}{\cos\delta(u + \dot{\psi} w_{\mathrm{f}}) + \sin\delta(\dot{\psi} a + v)}\right).
\end{aligned} \tag{A29}$$

The left-hand part of Figure A2 shows the load dependence of the longitudinal tyre force under pure longitudinal slip conditions; larger longitudinal forces are available when the normal load is increased. The right-hand part of Figure A2 shows how the longitudinal force is compromised when the tyre is side slipping. As the side-slip angle increases, the longitudinal peak force reduces and moves towards higher slip values.

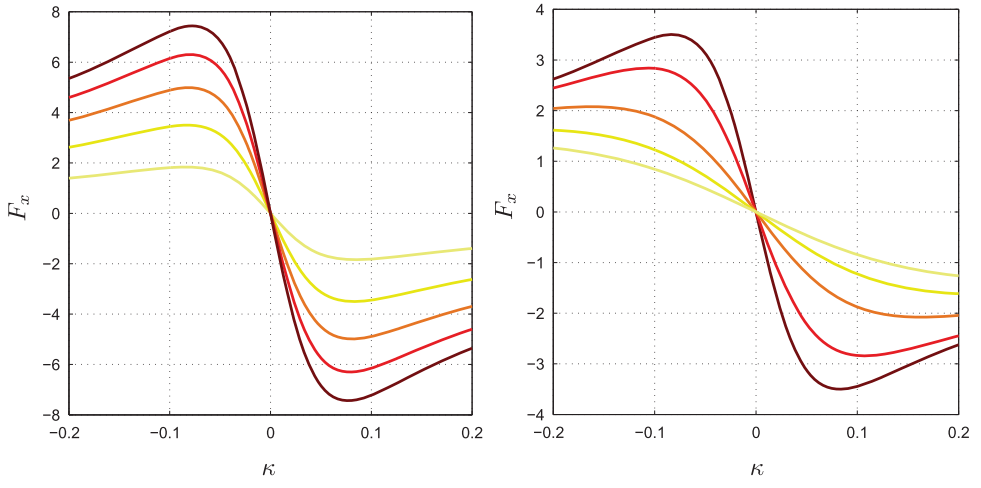

Figure A2. Longitudinal tyre force versus longitudinal slip (F_x is given in kN). The left-hand diagram considers five normal loads (at $\alpha = 0^\circ$); the lightest curve corresponds to 1000 N with the normal load then increased in steps of 1000 N. The right-hand diagram considers combined slip for five values of side-slip angle at a normal load of 2000 N; the darkest curve corresponds to a slip angle of 0° with the slip angle increased in steps of 5°.

Appendix 3. Vehicle and tyre data

This appendix contains nominal values for the tyre and vehicle parameters used in this paper (see Tables A1 and A2). The drag and down forces are given by

$$F_{ax} = -\frac{1}{2} C_D \rho A u^2, \tag{A30}$$

$$F_{az}^{\mathrm{f}} = \frac{1}{2} C_L^{\mathrm{f}} \rho A u^2, \tag{A31}$$

$$F_{az}^{\mathrm{r}} = \frac{1}{2} C_L^{\mathrm{r}} \rho A u^2, \tag{A32}$$

in which the f and r superscripts refer to the front and rear axles, respectively. The drag and down-force coefficients used in this study are given in Table A3. The air density is assumed to be $\rho = 1.2$ kg/m^3, whilst the car's frontal area is $A = 1.5\,\mathrm{m}^2$.

Table A2. Tyre friction parameters.

Symbol	Description	Value
F_{z1}	Reference load 1	2000 N
F_{z2}	Reference load 2	6000 N
μ_{x1}	Peak longitudinal friction coefficient at load 1	1.75
μ_{x2}	Peak longitudinal friction coefficient at load 2	1.40
κ_1	Slip coefficient for the friction peak at load 1	0.11
κ_2	Slip coefficient for the friction peak at load 2	0.10
μ_{y1}	Peak lateral friction coefficient at load 1	1.80
μ_{y2}	Peak lateral friction coefficient at load 2	1.45
α_1	Slip angle for the friction peak at load 1	9°
α_2	Slip angle for the friction peak at load 2	8°
Q_x	Longitudinal shape factor	1.9
Q_y	Lateral shape factor	1.9

Table A3. Speed dependant (u, in m/s) aerodynamic drag and downforce parameters, given as second-order polynomial coefficients in the form $a_2u^2 + a_1u + a_0$.

Coefficient	a_0	a_1	a_2
C_L^f	1.614	-1.392×10^{-3}	-4.165×10^{-5}
C_L^r	1.935	8.335×10^{-3}	-1.249×10^{-4}
C_D	1.053	-6.643×10^{-4}	-1.018×10^{-5}